Unconstrained Piezoelectric Vascular Electronics for Wireless Monitoring of Hemodynamics and Cardiovascular Health

Chuyu Tang, Zhirong Liu, Quanhong Hu, Zhuoheng Jiang, Mingjia Zheng, Cheng Xiong, Shaobo Wang, Shuncheng Yao, Yunchao Zhao, Xingyi Wan, Guanlin Liu, Qijun Sun, Zhong Lin Wang, and Linlin Li*

The patient-centered healthcare requires timely disease diagnosis and prognostic assessment, calling for individualized physiological monitoring. To assess the postoperative hemodynamic status of patients, implantable blood flow monitoring devices are highly expected to deliver real time, long-term, sensitive, and reliable hemodynamic signals, which can accurately reflect multiple physiological conditions. Herein, an implantable and unconstrained vascular electronic system based on a piezoelectric sensor immobilized is presented by a "growable" sheath around continuously growing arterial vessels for real-timely and wirelessly monitoring of hemodynamics. The piezoelectric sensor made of circumferentially aligned polyvinylidene fluoride nanofibers around pulsating artery can sensitively perceive mechanical signals, and the growable sheath bioinspired by the structure and function of leaf sheath has elasticity and conformal shape adaptive to the dynamically growing arterial vessels to avoid growth constriction. With this integrated and smart design, long-term, wireless, and sensitive monitoring of hemodynamics are achieved and demonstrated in rats and rabbits. It provides a simple and versatile strategy for designing implantable sensors in a less invasive way.

C. Tang, Q. Hu, M. Zheng, C. Xiong, S. Wang, Y. Zhao, G. Liu, Q. Sun, L. Li
Center on Nanoenergy Research
School of Physical Science & Technology
Guangxi University
Nanning 530004, China
C. Tang, Z. Liu, Q. Hu, Z. Jiang, M. Zheng, C. Xiong, S. Wang, S. Yao, Y. Zhao, X. Wan, Q. Sun, Z. L. Wang, L. Li
Beijing Institute of Nanoenergy and Nanosystems
Chinese Academy of Sciences
Beijing 101400, P. R. China
E-mail: lilinlin@binn.cas.cn
Z. Liu, Z. Jiang, S. Yao, X. Wan, Z. L. Wang, L. Li
School of Nanoscience and Engineering
University of Chinese Academy of Sciences
Beijing 100049, P. R. China
Z. L. Wang
Georgia Institute of Technology
Atlanta GA 30332-0245, USA

1. Introduction

Patient-centered healthcare has become increasingly critical in clinical medicine.[1] For patients requiring long-term care, real-time and accurate monitoring of physiological signals is essential for disease diagnosis and prognostic evaluation.[2] Traditional methods of monitoring single physiological signal, such as blood pressure, heart rate, and blood oxygen level are no longer sufficient to meet the increasing needs of diagnosis.[3] More and more vital sign indicators are being introduced into clinical practice to improve monitoring accuracy and prognostic clinical prediction.[4] Among them, hemodynamic parameters provide multitudes of information about the cardiovascular system, such as arterial status and cardiac function.[4a,5] The change of pulse waveforms can reflect the early disease progression of arteriosclerosis, so as to guide the treatment and monitor therapeutic effect.[6] Thus, sensitive and reliable sensors are urgently required to monitor physiological signals in a real time manner.[7]

Implantable pulse sensors enable real-time monitoring of hemodynamic parameters such as cardiac output and vascular resistance, providing critical physiological indicators for clinicians. Especially, with regards to the postoperative recovery of bypass surgery or organ transplantation, it can reflect the arterial status and blood supply of the surgical sites in real time, so as to find the lesions/thrombosis in time for guiding clinical decision-making.[1b,8] Recently, several classes of methods have been developed for obtaining physiological parameters of cardiovascular system,[9] including optical methods,[10] ultrasonic imaging,[1a] and mechanical sensing.[8a,11] Among them, the mechanical sensors can directly reflect the pressure waves by attaching them around artery.[12] However, traditional rigid sensors often suffer from problems of slippage or mechanical mismatch with the target tissues/organs, which will seriously discount their mechanical sensitivity and long-term monitoring stability, and might induce mechanical damage to the tissues.[13] In addition, their invariable dimensions may restrict the normal growth of
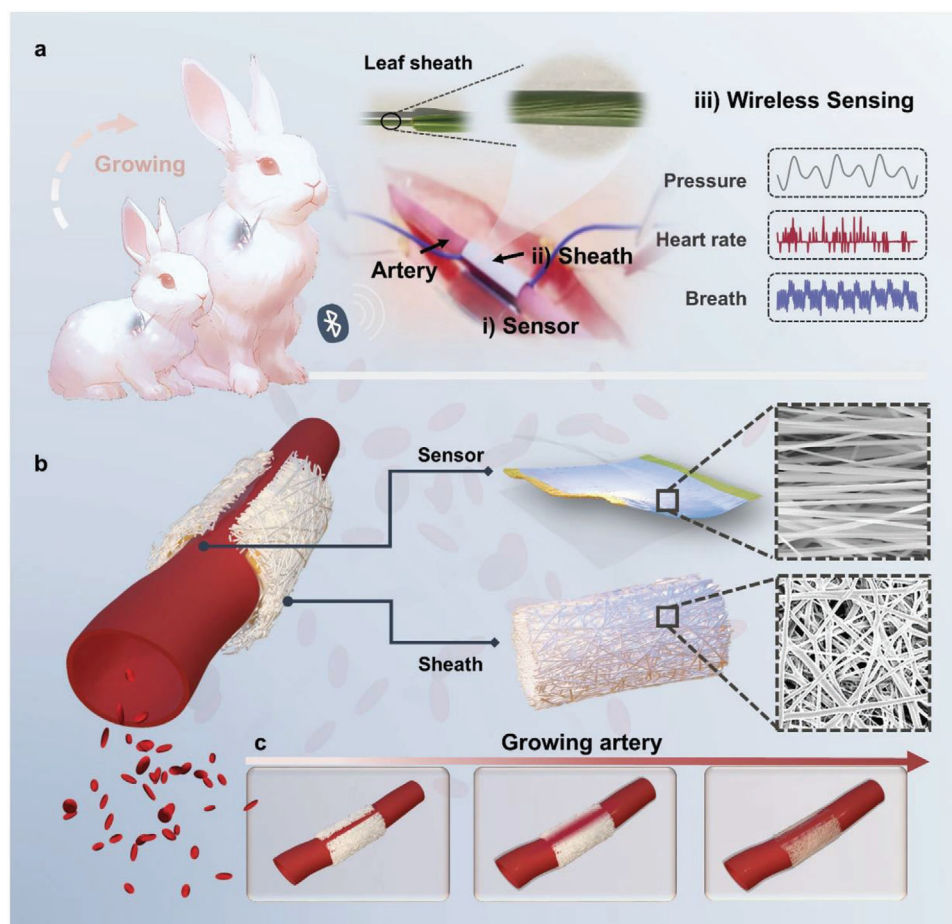
Figure 1. Overview of the unconstrained vascular electronic system. a) Illustration of the implantable electronic system, which includes: i) a flexible piezoelectric sensor for real-time hemodynamic monitoring; ii) a growable sheath for immobilization of the sensor around the artery; iii) a wireless data transmission and receiving module. b) A conceptual view of the sensing procedure: the sensor is implanted around the artery in an adapted shape with the sheath. c) Schematic diagram showing immobilization of the sensor with the growable sheath.

tissues especially for those growing bodies and tissues.[13] To overcome these problems, researchers have explored adaptable sensors, utilizing fully degradable materials,[8b,14] or optimizing the structures of the encapsulating materials[1b,15] to autonomously adapt to the tissue geometry. Despite these efforts, achieving multiple performance in implantable sensors has primarily relied on optimizing the sensor's composition and structure, resulting a trade-off and balance between different functions.[16] Consequently, the development of a strategy that integrates multiple functions without compromising various performance indicators remains a significant challenge for implantable sensor.[14b]

To meet the requirement of dynamic monitoring of growing vessels, herein, we present an implantable and unconstrained vascular electronic system for wireless hemodynamic monitoring based on a piezoelectric sensor and a biomimetic conformal sheath (**Figure 1**a).

This system utilizes circumferentially aligned polyvinylidene fluoride nanofibers (PVDF NFs) around the artery as the piezoelectric sensor unit, which enables sensitive and real-time monitoring of the lateral pressure changes of the vessel wall during blood flow. To secure the long-term monitoring stability and accu-

racy of the sensor, bioinspired by leaf sheath, we employ nanofibrous elastic polyurethane (PU) to fabricate a sheath for immobilization of the sensor, which can adaptively grow with the artery to avoid causing growth restraint (Figure 1b). By endowing the sensing system with tissue fit and "growable" performance through using the sheath, we were able to preserve the sensor's sensitivity to the greatest extent possible without compromising its strength. We demonstrate the sensitive and long-term monitoring of the sensor with the unconstrained immobilization strategy in rats and rabbits. As the animals grow from infancy to adulthood, the sheath ensures that the sensor is conformally attached to the surface of the growing artery for continuous hemodynamic monitoring, without interfering with the normal growth and function of the artery (Figure 1c). The acquired hemodynamic information is wirelessly transmitted to the mobile terminal for postoperative evaluation. Compared to traditional monitoring methods, our proposed system offers distinct advantages. First, the circumferentially aligned PVDF (aPVDF) NFs have high sensing sensitivity for monitoring multiple parameters including blood pressure, heart rate, and breath wave. Second, the growable sheath enables the sensor to adhere around artery as closely as a leaf sheath in nature, ensuring dynamic and precise

**ADVANCED
SCIENCE NEWS**

www.advancedsciencenews.com

**NANO · MICRO
small**

www.small-journal.com

monitoring without restricting the normal growth of artery. Third, it realizes wireless and battery-free monitoring, which can effectively miniaturize the implanted devices and solve the problem of frequent battery replacement, lowering the risk of infection and discomfort of patients.[17] This work provides a simple and universal strategy for designing low-invasive, implantable, and sensitive electronics.

2. Results and Discussion

2.1. Overview of the Vascular Electronic System

The implantable and unconstrained vascular electronic system consists of three parts: i) a flexible piezoelectric sensor for real-time hemodynamic monitoring; ii) a tensile tubular sheath with open ends that for immobilizing the piezoelectric sensor around artery to ensure long-term stable monitoring without restricting the normal growth of the artery; and iii) a wireless module for power supply and data transmission (Figure 1a). The flexible and ultrathin piezoelectric sensor is made from highly aligned PVDF nanofibrous film that is electrospun using a parallel plate electrode receiver (Figure S1, Supporting Information). Gold electrodes are magnetron sputtered at both ends of the PVDF nanofibrous film, and the whole sensor is hot-press encapsulated by medical flexible PU tape (**Figure 2**a). The resultant piezoelectric sensor with a total thickness of 78 μm is wrapped around artery, with the aligned nanofibers along the circumference of the artery. This architecture can empower the sensor to sensitively perceive subtle mechanical forces during blood flow for electro-mechanical conversion and hemodynamic monitoring, outputting blood pressure, heart rate, and breath wave. The biomimetic sheath fabricated from elastic nanofibrous PU tube assists to immobilize the sensor on the arterial surface. With open ends and elasticity, it can adaptively grow with the artery, thereby eliminating the stress at the interface between the sensors and the growing artery for ensuring long-term and stable monitoring. The acquired raw data are wirelessly transmitted through the Bluetooth module after signal amplification and filtering, and displayed in real time on the customized APP of mobile phone.

From the scanning electron microscopy (SEM) images in Figure 2b, aPVDF NFs are highly aligned along one direction. For comparison, random PVDF (rPVDF) NFs were also fabricated with random-arranged nanofibers. Fourier transform infrared spectroscopy (FT-IR) results indicated that nonpiezoelectric α phase (532, 613, 762, 870, and 976 cm^{-1}) and piezoelectric β phase (486, 509, and 839 cm^{-1}) coexisted in the PVDF NFs (Figure 2c).[18] In comparison, aPVDF NFs had a higher β-phase content than rPVDF, due to their better stretching and polarization using parallel plate electrode receiver during electrospinning.[19] We used thermal annealing treatment to further improve the piezoelectricity of aPVDF. From the X-ray diffraction (XRD) patterns (Figure 2d), the β-phase content in aPVDF NFs enhanced gradually with the increase of annealing temperature from 60 to 135 °C (Figure S2, Supporting Information). The highest β-phase content was observed in aPVDF NFs annealed at 135 °C, with a calculated value of 66.61% obtained by Gaussian peak fitting analysis of the XRD patterns, in sharp contrast to the 30.63% in the unannealed aPVDF NFs.

Piezoelectric force microscope (PFM) was utilized to explore the behavior of ferroelectric hysteresis and piezoelectric electromechanical behavior in nanofibers (Figure 2e,f). Initial PFM testing provided vertical PFM amplitude and PFM phase images of a single fiber. Subsequently, the piezoelectric response of a single nanofiber was measured under an alternating voltage. The results exhibited a distinct butterfly-shaped amplitude-voltage hysteresis loop, confirming its piezoelectricity. Under bias voltages of +5 and −5 V, the nanofiber displayed amplitudes of 0.26 and 0.15 nm, respectively, validating the piezoelectric property of the PVDF nanofiber. Additionally, the observed phase-voltage hysteresis loop confirmed the ferroelectric properties of the sample. Those small amplitude changes in the hysteresis loop may be attributed to dimensional or polarization alterations in the fiber influenced by the electric field. Besides its excellent piezoelectric property, the nanofibers of aPVDF arranged along the circumference of the artery were more conducive to sensing the expansion and contraction of blood vessels during blood flow (Figure S3, Supporting Information). Thus, aPVDF was employed as the sensing unit to fabricate the piezoelectric sensor. From results of the tensile experiments, the original aPVDF NFs were almost unstretchable, whereas the sensor hot-press encapsulated with the elastic PU film had enhanced strain-tensile stresses (Figure 2i), which was beneficial to mechanical matching with arteries and reducing tissue constraints.

The long-term stable matching of implantable sensors with local tissues especially growing tissues determines their sensing accuracy and biosafety.[1b] The biomimetic sheath can enclose the sensor around the artery, preventing it from sliding off from the tissue. Its structure and function is similar to leaf sheaths that protect shoots and provide mechanical support to the stems (Figure 1a). The sheath design enables convenient, fast, and reliable operation, without need for additional tools or adhesives that might induce tissue mismatching and damage. The sheath was fabricated by simply cutting open the electrospun PU tube along the direction of the extension axis. From the SEM image in Figure 2g, the nanofibrous PU tube had rough and porous surface morphology, bionic to the connective tissue structure of vascular adventitia.[20] To improve the hydrophilicity for cell and tissue growth in for strengthening the immobilization, we treated it with oxygen plasma, after which process the water contact angle reduced from 83.7° ± 2.1° to 23.0° ± 2.7° (Figure 2h; and Figure S4, Supporting Information). The breathability of the electrospun PU was characterized through a water vapor transmission rate (WVTR) test, which showed high gas permeability, avoiding potential inflammatory response of the electronics during its long-term implantation (Figure S5, Supporting Information). The tensile properties of the sheath were also considered for better biomechanical matching with living tissues. Throughout 1000 cycles of tensile testing with a strain of 50%, both the sensor (Figure 2i) and the sheath (Figure 2j) consistently demonstrated resilience to the applied stress loading and unloading during each stretching cycle, with minimal hysteresis, indicating the excellent mechanical stability and ability to sustain physiological pressure changes. Through mechanical simulations, we investigated the adaptability of the leaf sheath structure to accommodate its growing contents. By conducting finite element dynamic mechanical simulations (Figure 2k), we observed that
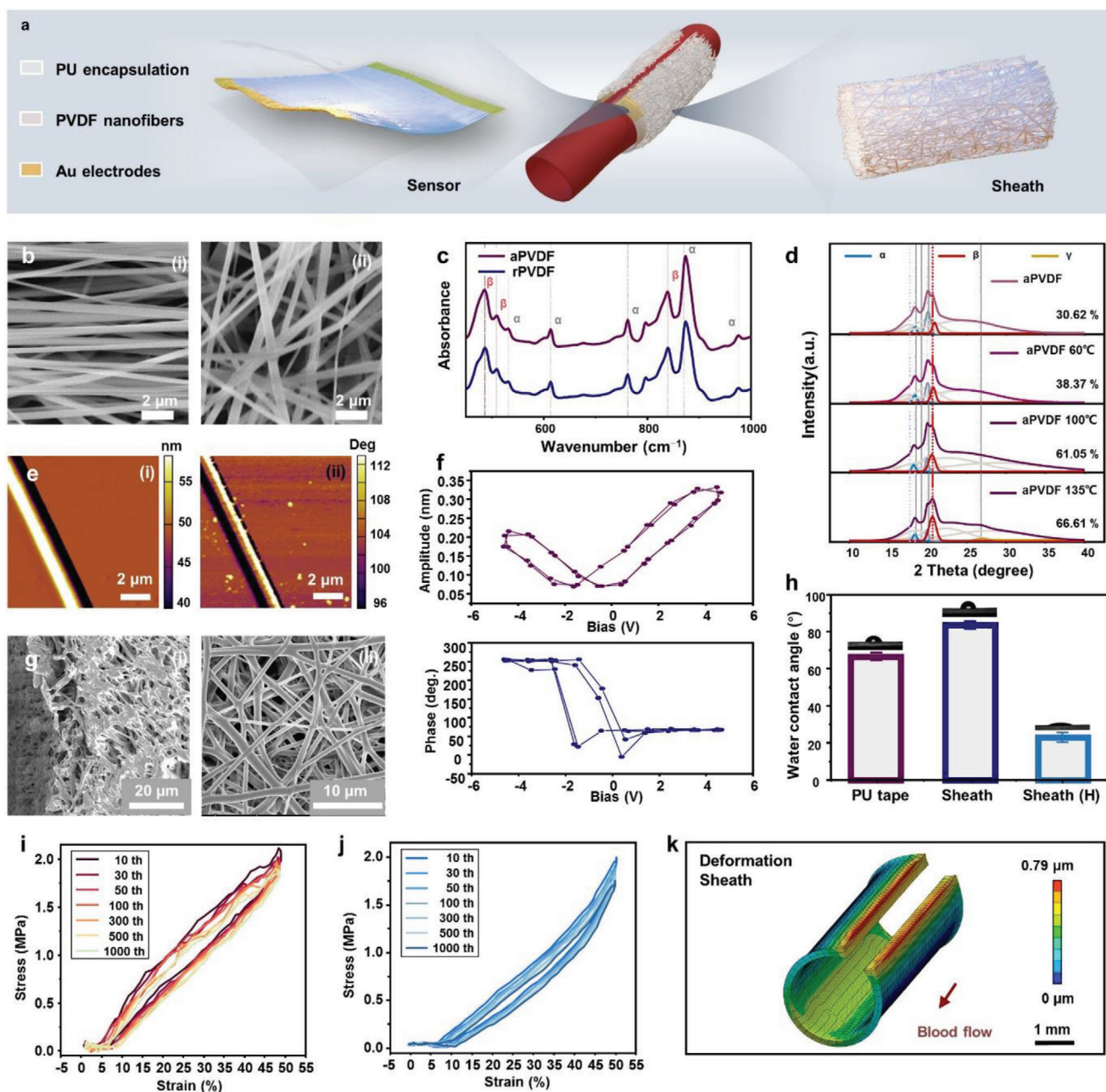
Figure 2. Fabrication and characterization of the unconstrained vascular electronic system. a) Exploded schematic diagram of the sensor immobilized on the arterial surface by the sheath. b) SEM images of the (i) aPVDF and (ii) rPVDF NFs. c) FT-IR spectra of the PVDF NFs. d) XRD spectra of the as-prepared aPVDF NFs and aPVDF NFs after annealing at different temperatures. e) (i) AFM topography and (ii) PFM phase image of the single aPVDF nanofiber. f) Amplitude and phase hysteresis loop of the aPVDF nanofiber. g) SEM images of i) cross-sectional view and ii) surface view of the nanofiberous PU tube for fabricating the sheath. h) Water contact angle and statistic results, $n \geq 5$. i) Stress–strain curves of the piezoelectric sensor at different cycles. j) Stress–strain curves of the PU tube at different cycles. k) Finite Element Analysis illustrating stress distribution in open PU tubes under pulsatile circumferential forces.

the open-ended tubular design of the sheath resulted in stress concentration areas near the opening due to the disrupted symmetry. As the artery dimeter changes during growth, the sheath opening expands accordingly. Consequently, it exhibits produce greater deformation under the same external force, allowing the sheath to dynamically adapt to changes in vessel size, which can be considered as "growth" for this system. The increased compliance ensures flexible adaptation of the sheath to accommodate varying sizes of its contents. Building upon these observations, we further examined the impacts of sheath area, thickness, and porosity on fixation stability and vascular compliance. Figure S6 (Supporting Information) provides additional insights into these factors, which hold significant guiding for sheath design consideration.
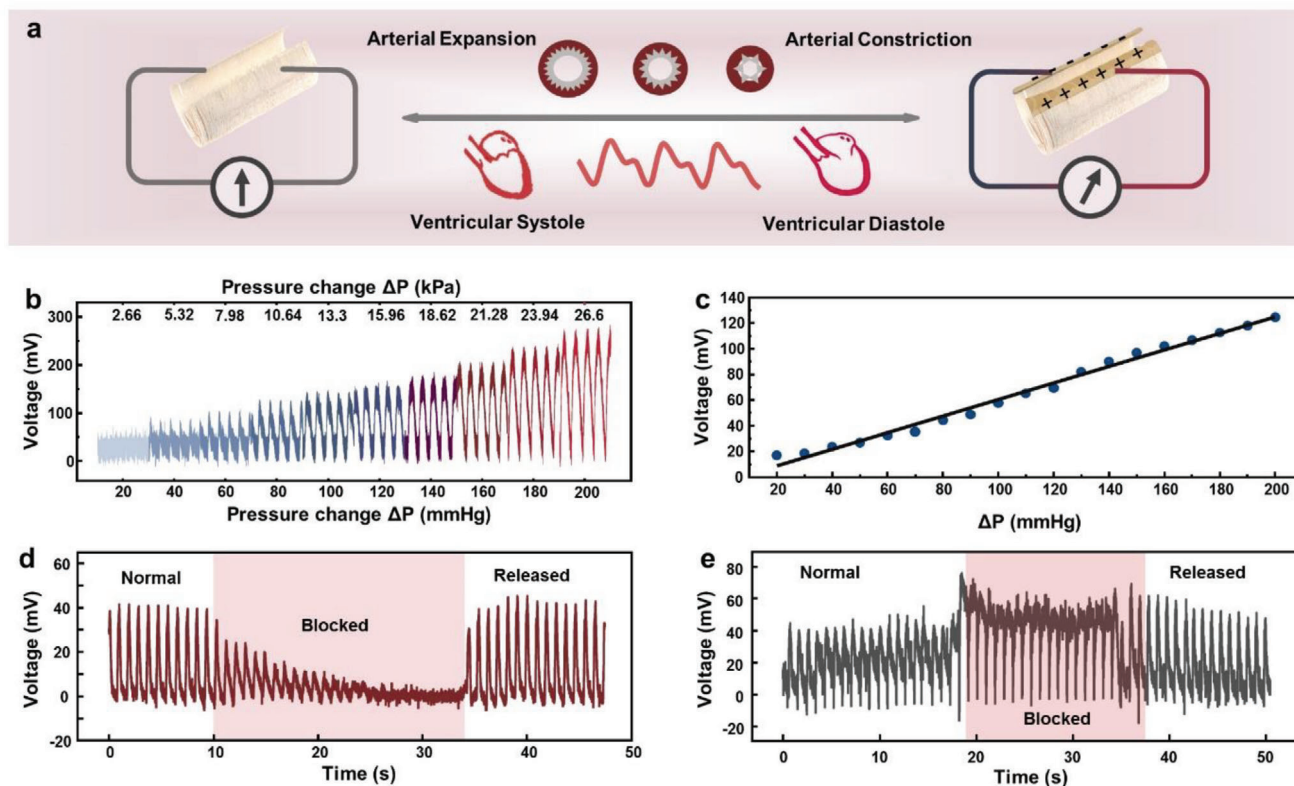
ADVANCED
SCIENCE NEWS
www.advancedsciencenews.com

NANO · MICRO
small
www.small-journal.com

Figure 3. In vitro hemodynamic sensing of the piezoelectric sensor using a simulated vascular access. a) Schematic diagram of the sensing mechanism. b) Voltage output of the sensor under different internal pressures. c) Linear fit of the voltage outputs under different internal pressures. d,e) Voltage output of the sensor that was positioned sequentially at d) the distal and e) proximal ends of the embolism.

2.2. In Vitro Validation of the Hemodynamic Sensing

To validate the hemodynamic sensing properties of the piezoelectric sensor, we constructed a three-way system to mimic the pulsatile behavior of the artery in vitro. It was consisted of a simulated vascular access, a standard sphygmomanometer and a compressible balloon. The volume of the balloon was compressed by a linear motor to adjust the pressure of the whole passage, and the balloon was repeatedly pressed and released at low frequencies to simulate the regular pulsation of heart. A standard sphygmomanometer was employed to reflect the pressure of the simulated vascular access (Figure S8, Supporting Information). The piezoelectric sensor was wrapped around the artificial blood vessel (diameter of 5 mm) with a matching sheath. As illustrated in **Figure 3**a, when fluid is pumped through the artificial blood vessel, it expands and compresses the surface-attached piezoelectric sensor, thus generating a piezopotential across the piezoelectric PVDF NFs for hemodynamic sensing.

We first established the relationship between the voltage outputs and the pressures. With the increase of simulated intravascular pressures (20–200 mmHg, 1 Hz), the output voltages increased correspondingly, reaching a significant linear relation (R^2 = 0.99) and a high sensitivity of 0.64 mV mmHg^{-1} (Figure 3b,c), preliminarily validating the reliability of the sensor for monitoring intravascular pressure. We performed a hemodynamic analysis on a segment of a blood vessel with 70% thrombotic stenosis using a fluid–solid coupling analysis (Figure S9, Supporting Information). The results indicate that the local pressure difference caused by the stenosis at both ends of the diseased vessel is significantly higher compared to a normal vessel. Additionally, there is a larger drop in blood pressure at the distal end of the stenotic site. Therefore, continuous monitoring of the local arterial blood pressure can serve as an indicator of changes in the condition. To verify the ability of the sensor to monitor the pathological states of common cardiovascular diseases, we constructed an arterial stenosis model by selecting a prepositioned ischemia, and positioned the sensor near and far away from the pump (simulated heart), respectively. We used the wire plug method to control the blockage at the prepositioned embolic point. From the results in Figure 3d, the distal sensor can respond sensitively to embolism degree, as displayed by a gradual weakening of the output voltages and a rapid recovery after unbinding. For the proximal sensor, the voltage waveform changed and the signal deteriorated when the embolism degree was enhanced, which was due to the increase in simulated intravascular pressure caused by the decrease in rheological volume (Figure 3e). These results of the in vitro models verified that the piezoelectric sensor can reflect the changes in internal lumen pressure real-timely, which can help to diagnose embolism and locate the embolism sites.
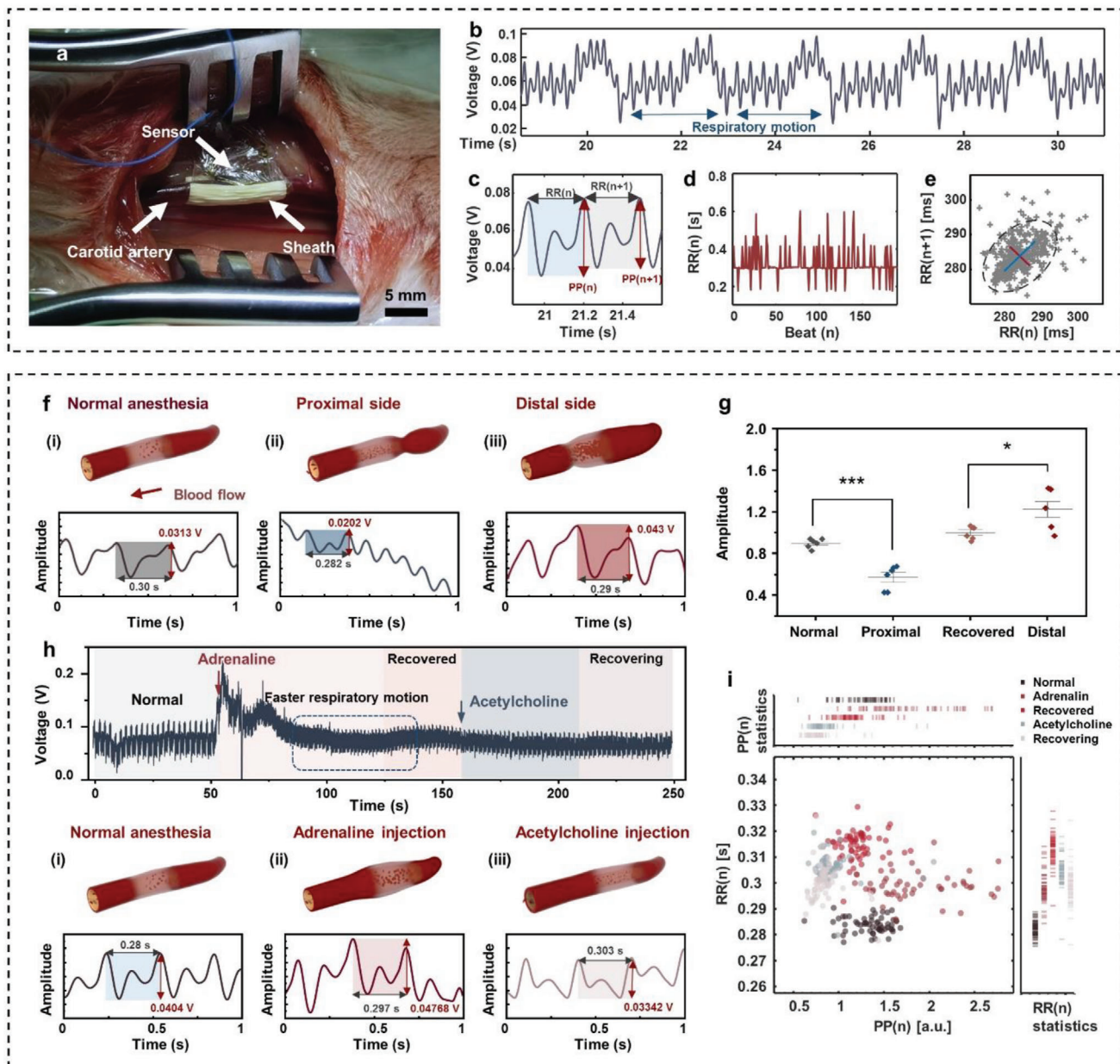
Figure 4. Real-time hemodynamic monitoring with the unconstrained vascular electronic system and dynamic regulation of the physiological status in rabbits. a) The sensor was implanted surrounding the carotid artery of a rabbit and immobilized by a sheath. b) Pulse waves under anesthesia. c) Information extracted from the pulse wave signals. d) Heartbeat interval (RR interval) under the action of anesthesia. e) Pioncare plots of RR interval under the action of anesthesia. f) Pulse waves in stenosis model. g) Pulse wave amplitude in stenosis, $n \geq 6$, *** represents $p < 0.001$, * represents $p < 0.05$. h) Pulse waves under different physiological regulation conditions. i) Scatter plot of pulse wave amplitude versus RR interval, where $n \geq 60$ for each group.

2.3. In Vivo Validation in Rabbits

When the heart contracts and pumps blood into the arteries, pressure wave will be generated in the arteries, presented as pulse wave. The implanted piezoelectric sensor can sense the pressure changes caused by expansion and contraction of the arteria, so as to evaluate the cardiovascular health. We first implanted the sensing system into rabbits. As shown in **Figure 4**a, the sensor was attached to the carotid artery of the rabbits

and immobilized with the sheath. From the real-time output voltage of the sensor, pulse waves in carotid artery and respiratory waves can be accurately distinguished (Figure 4b; and Video S2, Supporting Information). Moreover, detailed arterial pulse wave information, including pulse pressure (PP), rise time, decay time, and heartbeat interval (RR interval) can be analyzed (Figure 4c). Under an anesthesia situation, the heart rate variability was relatively stable from the statistical results (Figure 4d,e).

To verify that the sensor can accurately monitor dynamic changes of the hemodynamic parameters for reflecting physiological and pathological states, we constructed a local artery occlusion model and a body fluid regulation model in the rabbits. We first simulated the peripheral stenosis through extravascular ligation during implantation. At the distal end of the stenosis, the blood flow slowed down and the pulse waves formed a relatively flat crests, so that the amplitude changes of the pulse waves were relatively small and the output signal was lower than normal. When the vessel was completely constricted, blood flow was mechanically blocked and the signal intensity almost faded. At the proximal end of the stenosis, due to the elasticity of the artery, there is often reflux as blood flows through the stenosis, causing the inner wall of the vessel to deform outward. This created a waveform peak that resulted in an increase in the pulse waves. The signal amplitude also increased progressively with the degree of stenosis (Figure 4f,g; and Figure S10, Supporting Information).We used physiological regulation drugs of adrenaline and acetylcholine to modulate the cardiac electrophysiology, respectively. Figure 4h; and Figure S6 (Supporting Information) shows the pulse wave changes following the administration of adrenaline and acetylcholine, respectively. Under normal anesthesia, the pulse waves had less variability in frequency and amplitude, with heart rate variability (HRV) of 0.12 and blood pressure variability (BPV) of 0.32 (Figure S11, Supporting Information). The scatter plot of pulse interval and amplitude also showed an accumulation of dot clusters (Figure 4i). With the action of adrenaline, the signal amplitude increased and the pulse wave frequency decreased. The corresponding HRV and BPV increased to 0.33 and 0.71, respectively, with a corresponding increase in respiratory rate (Figure S10, Supporting Information). The horizontal scatter projection of the pulse wave amplitude showed an irregular pattern with large oscillation in the direction of the amplitude enhancement. This result was in agreement with the adrenaline elicited heart inotropic and lusitropic response. As the body recovered from the drug action, the scatter points tended to concentrate in the direction of weakening amplitude, indicating that the cardiovascular function was recovered (Recovered stage in Figure 4i). Compared with the initial normal state of anesthesia, the slopes of the epinephrine effect scatters rose first and then decreased during the recovery stage (Figure S12, Supporting Information), indicating a decrease in vascular elasticity and sensitivity as a result of the body's regulation of the overall vascular system in the case of persistent hypertension.[21]

After the body was recovered from the action of adrenaline, acetylcholine was subsequently injected intravenously. From Figure 4h(iii), the signal amplitudes decreased and the pulse wave intervals lengthened, with a corresponding decrease in heart rate. The BPV changed from 0.1645 (Recovered stage) to 0.27 and the HRV value was 0.48. In addition, dispersion reappeared in the horizontal scatter projection, indicating the interfered physiological function by acetylcholine. As time went on, the scatter projections in all directions tended to be concentrated back, corresponding to BPV and HRV of 0.25 and 0.27, respectively (Recovering stage in Figure 4i). And the slope of the scatters shifted to be steeper, reflecting the recovery of the Baroreflex sensitivity (BRS) and the new homeostasis of body function. These results demonstrated that the sensor can monitor the hemodynamics in real time and accurately reflect the physiological and pathological states.

2.4. Long-Term Hemodynamic Monitoring in Rats

To verify the feasibility of long-term monitoring, we implanted the whole unconstrained vascular electronic system including a piezoelectric sensor, a sheath, and a wireless module into SD rats over a time course of 10 weeks, during which the rats grew from adolescent rats to adult (**Figure 5**a; and Figure S9, Supporting Information). After implantation of the system, all the SD rats survived without obvious behavioral difference (Figure S10, Supporting Information). As observed from the optical photograph (Figure 5b) and micro-CT imaging (Figure 5c) results, the sensor was closely attached to the abdominal aorta of the rat with the assist of the sheath, and the whole system was completely implanted in the abdomen of rats. In this system, the piezoelectric sensor was self-powered and driven by the animal activities, and the data transmission module implanted in abdomen was powered by a subcutaneous wire coil through wireless charging technology based on electromagnetic induction. Thus, the whole system did not need batteries, which was beneficial to improving its biocompatibility and convenient applications. The electric signals are transmitted wirelessly, making it suitable for long-term applications. As shown in Figure 5d, the pulse waveforms of the abdominal aorta were displayed on a mobile phone in real time, with excellent signal quality. The application of the PU sheath resulted in an improved signal-to-noise ratio (SNR), which increased from 28.64 to 31.17 dB (Figure S15, Supporting Information). Moreover, accurate monitoring could be performed for over 10 days (Figure 5e; and Figure S16 and Video S3, Supporting Information). The Bluetooth signal transmission module consumes an average power of 0.13 W during its operation, which can be conveniently provided by the wireless charging mode.

We evaluated the effect of the system on the vascular function of growing arteries after implantation of the system into the abdominal aorta of adolescent rats (weight of 150–200 g, 8 weeks old) for a time course of 10 weeks. We selected several time points during the rat growth to display the state of the sensing system, stage I (200–250 g, 10 weeks old), stage II (300–350 g, 13 weeks old), and terminal stage (400–450 g, 18 weeks old). All through the whole process. The piezoelectric sensor was always wrapped by the sheath and attached to the surface of the artery (Figure 5f). Results of hematoxylin-eosin (H&E) and Masson's trichrome staining of the tissue sections (Figure 5f; and Figure S17, Supporting Information) showed that at all the stages the vessel had normal morphology without obvious inflammation or hyperplasia. Masson staining revealed a significant number of collagen fibers entirely encompassing the sheath, with limited infiltration of inflammatory cells and interspersed fibroblasts within the collagen fibers (Figure S17, Supporting Information). The presence of the protective fibrous layer (Figure 5f) indicated successful implant-tissue integration that further facilitated the sensor immobilization, improving the sensing stability and reducing the possible adverse effect on the artery.

Based on the H&E staining results, the abdominal aortic midline circumference, wall area, mean thickness, and corresponding diameter of arteries were counted ($n = 3$). With the animal
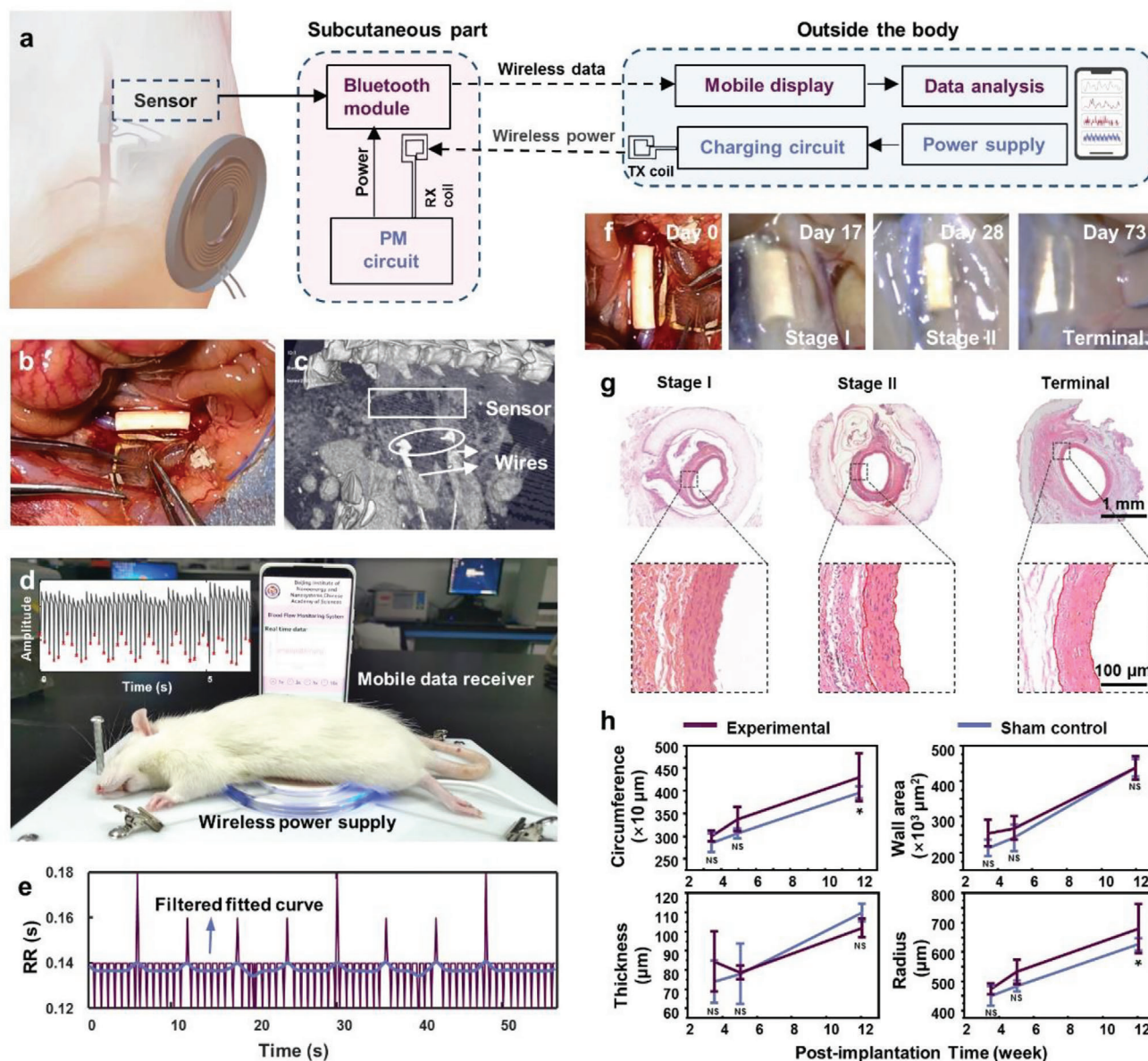
Figure 5. Long-term implantation, sensing, and biocompatibility of the unconstrained vascular electronic system in rats for wireless hemodynamic monitoring with battery-free power supply. a) Block diagrams of the wireless system. PM circuit: power management circuit; TX coil: transmitter coil; RX coil: receiver coil. b) Optical photograph of the surgery in rats for implantation of the system. c) CT imaging of the rat after implantation of the electronic system. d) Optical photograph shows the real-time acquisition and display of the pulse wave signals on a mobile phone. e) The rat's pulse RR interval on day 10 after the implantation. f) Photographs showing the state of the system at different stages. g) H&E staining images and h) statistics for arterial midline circumference, wall area, arterial thickness, and radius. $n \geq 3$ for each group; NS represents no significant; * represents $p < 0.05$.

growth, all these indexes tended to increase, and had consistent changing trends and values compared to the control group. It implied that our sensing system had favorable biocompatibility and the long-term implantation did not affect the normal vascular growth and function (Figure 5g,h). We also collected the major organs (heart, liver, spleen, lungs, and kidneys) of the rats for evaluating the influence on them. There was no obvious injury or inflammation of these tissues (Figure S18, Supporting Information). Meanwhile, all the indexes in routine blood tests were within the normal range after 4 weeks of implantation. And the

blood biochemical assay results indicated that there were no abnormal changes in myocardium, liver, and renal function in all the rats (Figure S19, Supporting Information).

In light of this, the implantable unconstrained vascular electronic system is expected to be used as part of an intelligent mobile follow-up system, which provides an end-to-end solution that allows continuous acquisition of the hemodynamic information. Through detecting the amplitude and frequency of the blood pressure fluctuation in arterial lumen, the condition of arteries can be monitored in real time during intraoperative or

**ADVANCED
SCIENCE NEWS**

www.advancedsciencenews.com

**NANO · MICRO
small**

www.small-journal.com

postoperative follow-up. Furthermore, this technology is independent of the operators' skill level and environment, providing more stable and reliable measurements than traditional pulse detection methods. Powered by Wireless Power Transmission system, the sensing system also eliminates the need for batteries, thus reducing the size and weight of the overall system for improving patients' acceptance and compliance. This integrated, wireless, and unconstrained vascular sensing system enables long-term physiological monitoring, which can be linked to networks and smart terminals for daily health assessment, promising in online monitoring and smart mobile diagnosis for prevention of cardiovascular disease.

3. Conclusion

This work proposes a mechanical reinforcement and adaptive strategies for addressing the mechanical mismatch or attachment problem of flexible sensors on growing tissues. With the bioinspired design of sheath allowing the flexible piezoelectric sensor to be mechanically coupled with the soft and growing artery, real-time, high-precision, and long-term hemodynamic sensing has been realized. Both in vitro and in vivo experimental results have verified the reliability and safety of the sensing system for hemodynamic monitoring, realizing real-time hemodynamic monitoring and display of cardiovascular conditions. This system has significant potential for postoperative rehabilitation evaluation of patients with cardiovascular diseases, such as aneurysms or atherosclerosis, making postoperative follow-up more convenient and efficient. This "growable" and unconstrained sheath design can also be used for designing other kinds of bioelectronics, for improving treatment outcomes and the patients' quality of life.

4. Experimental Section

Fabrication of PVDF NFs and PU Sheath: The aligned and random PVDF nanofibers were prepared by electrospinning process. Briefly, a mixture of dimethylformamide (DMF)/acetone (3:2 by volume) was used as the solvent. PVDF solution with a concentration of 20 wt% was prepared by dissolving PVDF tablets (M_w = 27 KDa, Sigma-Aldrich) in DMF/acetone solvent under continuous stirring. Then, it was loaded in a plastic syringe with a 21G steel needle, and a syringe pump was employed to control the flow rate at 1 mL h^{-1}. A fixed voltage of 20 kV was adopted between the syringe needle and the fiber collector with the working distance of 15 cm. The receiving device with two parallel electrodes was designed to collect the aligned PVDF nanofibers (Figure S1, Supporting Information), whereas a flat aluminum plate was employed to collect the random PVDF nanofibers. The thickness of the nanofibrous film was tailored through controlling the collection time. Then, the PVDF nanofibers were annealed overnight at different temperatures to increase the crystallinity.

The PU nanofibrous tube are made by collecting nanofibers using tube receivers with various diameters. A mixture of dichloromethane/DMF (1:3 by volume) was used as the solvent. The 37.5 wt% PU solution was prepared by continuous stirring of polyurethane pellets (M_w = 90 KDa) in dichloromethane/DMF solvent for 6 h at room temperature. It was then loaded in a plastic syringe with a 21G steel needle and a syringe pump was used to control the flow rate at 1 mL h^{-1}. A fixed voltage of 18 kV was used between the syringe needle and the fiber collector with a working distance of 15 cm. Subsequently, the electrospun PU fiber samples were placed in an oven at 60 °C to remove residual solvent and after 2 h the samples were stripped from the tube receiver. To improve their hydrophilicity for facili-

tating cell attachment, the samples were treated with oxygen plasma (in an oxygen flow rate of 50 sccm and a power of 50 W) by Plasma Cleaning System (PVA TePla/IoN 40, America) for 90 s. The water contact angle was acquired on XG-CAMB1, Xuanyi. Finally, the sheath was obtained by cutting open the electrospun PU tube along the direction of the extension axis.

The morphology of the nanofibers was characterized by the field-emission SEM (SU8020, Hitachi). FT-IR spectra were tested by Vertex80V (Bruker Corp., USA) ranging from 400 to 2000 cm^{-1}. XRD patterns were acquired on a Bruker D8 Advance powder XRD with Cu Kα radiation (λ = 0.15 406 nm). PFM measurements were performed at the modulation frequency equipped with external lock-in amplifiers (HF2LI, Zurich Instruments, Switzerland). A universal tensile testing machine (YL-S71, Yuelian) was used to perform the mechanical tests. The test scale length was 15 mm and the stretching speed was set at 10 mm min^{-1} until fracture of the samples.

Water Vapor Transmission Rate, WVTR Test: The electrospun PU with and without plasma treatment were affixed to the openings of 20 mL glass bottles. Open glass bottles served as a control group for evaporation, each with a diameter of 12 mm. The mass changes inside the bottles were monitored in a 60 °C oven.

Encapsulation and System Integration: The gold electrodes (thickness of ≈20 nm) on both ends of the PVDF sensor were magnetron sputtered onto aPVDF nanofibrous film using a mask. Flexible medical PU tape (Corfu Medical) was used for hot-press encapsulation, and pure silver wire with a diameter of 100 μm was used as the connecting wire. The Bluetooth transmitter and other acquisition back-end hardware were encapsulated in a 3D printed housing (13 mm × 24 mm × 8 mm), sealed with hot melt glue for waterproofing, and then vapor-plated with an ≈3 μm parylene film throughout for insulation and improving biocompatibility.

Three-Way System: A three-way system was built to simulate the blood flow and test the blood pressure monitoring ability of the sensor in vitro. It included a standard medical mercury column pressure gauge, a balloon controlled by LinMot linear motor (LinMot USA, Inc., Elkhorn, WI) as the pump, and a simulated vascular access to mimic the pressure changes inside the blood vessels. The effective working area of the PVDF sensor in the test was 1 × 1 cm^2, and a Keithley electrometer 6514 was used to record the output voltage. Air was directly used as the pressure transmission medium, and the pressure transmission tube was directly connected to the standard blood pressure monitor, with the other end connecting to a drainage gas collection device to replace the medium in the elastic artificial blood vessel with deionized water. Medical rubber tubing and three-way tubing were used to connect the sensor to the standard medical mercury column pressure gauge and pressure generator. Calibration began at a starting point of 20 mmHg (≈2.66 kPa), and an increment of 20 mmHg (≈2.66 kPa) was used as detection points for increasing pressure calibration.

Animals and In Vivo Studies: Animals were provided by Beijing Charles River Laboratories, and the procedures for handling the animals firmly stick to the national standards "Laboratory Animal Requirements of Environment and Housing Facilities (GB 14925-2001)." The animal experiments were approved by the Committee on Ethics of Beijing Institute of Nanoenergy and Nanosystems (Approval Number: 2022A039).

New Zealand rabbits were used in this study (aged 200–300 days, weighing 3–4 kg). For anesthesia, 30 mg kg^{-1} of 3% (30 mg mL^{-1}) sodium pentobarbital solution was injected through the ear vein. The hair around the rabbit's neck was removed after disinfection. The epidermis was incised to expose the left carotid artery for dissociating it. After the sensor was implanted, 5-0 absorbable sutures (Shanghai Pudong Jinhuan Medical Products Co., Ltd.) were used to close the incision. Then, adrenaline (1:10 000, 0.1 mL kg^{-1} body weight) and acetylcholine (1:10 000, 0.1 mL kg^{-1} body weight) were infused intravenously to temporarily adjust blood pressure and heart rate to verify the dynamic monitoring ability of the sensor. The generated voltage signals from the sensor were measured by a Keithley 6514 meter (Tektronix Inc., Beaverton, OR). Real-time acquisition and analysis of the pulse wave signal was based on Labview and MATLAB. After the surgery, the rabbits were treated with penicillin (800 000 units per day) for 3 days and were fed normally.

SD rats (starting at 7–8 weeks of age and weighing 150–200 g) were used in this research. The rats were fasted for 12 h before the surgery. Then, 0.35 mL of 2% (20 mg mL^{-1}) pentobarbital sodium solution was injected into the abdominal cavity. After disinfecting the abdominal hair with iodine, the rats' skin was incised, and the abdomen was opened to expose the abdominal aorta. The piezoelectric sensor was carefully wrapped around the outside of the rat's blood vessel using a PU sheath ($n = 9$). Six rats were used in the sham control group, in which the abdomen of the rats was opened and sutured, but no device was implanted. The wireless signal transmission module and the charging module were buried under the skin. Then, the incision was closed with 5-0 absorbable sutures. After the implantation, signals were collected using the Keithley electrometer 6514 (Tektronix Inc., Beaverton, OR) or wireless system. After the surgery, each rat was injected with 40 000 units of penicillin to prevent infection and allowed free access to food and water.

Long-Term Biocompatibility in Rats: Four weeks after the implantation of the sensing system, 2 mL of blood samples were collected from the SD rats for routine blood and biochemical tests. After 2, 4, and 12 weeks of the implantation, the internal abdominal aorta and major organs, including the heart, liver, spleen, lungs and kidneys were collected in all experimental groups. At the same time, 2 rats in the sham control group at the same stage also followed the same procedures. All the samples were preserved separately in 4% aqueous paraformaldehyde solution. Following the standard protocol, paraffin-embedded cross-sections of the arteries and major organs were stained with H&E and Masson's trichrome. Images were captured using an upright microscope (DM4000M, Leica, Germany). All images are representative of at least three independent samples.

Statistical Analysis: All statistics are reported as mean ± standard deviation and the number of groups is given in the figure caption. Data were compared between multiple groups using unpaired Student's *t*-test and between two groups using *t*-test and *$p < 0.05$ was considered statistically significant.

Supporting Information

Supporting Information is available from the Wiley Online Library or from the author.

Acknowledgements

Conflict of Interest

The authors declare no conflict of interest.

Data Availability Statement

The data that support the findings of this study are available in the Supporting Information of this article.

Keywords

[1] a) C. Wang, B. Qi, M. Lin, Z. Zhang, M. Makihata, B. Liu, S. Zhou, Y. H. Huang, H. Hu, Y. Gu, Y. Chen, Y. Lei, T. Lee, S. Chien, K. I. Jang, E. B. Kistler, S. Xu, *Nat. Biomed. Eng.* **2021**, *5*, 749; b) J. Shin, Y. Yan, W. Bai, Y. Xue, P. Gamble, L. Tian, I. Kandela, C. R. Haney, W. Spees, Y. Lee, M. Choi, J. Ko, H. Ryu, J. K. Chang, M. Pezhouh, S. K. Kang, S. M. Won, K. J. Yu, J. Zhao, Y. K. Lee, M. R. MacEwan, S. K. Song, Y. Huang, W. Z. Ray, J. A. Rogers, *Nat. Biomed. Eng.* **2019**, *3*, 37; c) F. Tasnim, A. Sadraei, B. Datta, M. Khan, K. Y. Choi, A. Sahasrabudhe, T. A. Vega Gálvez, I. Wicaksono, O. Rosello, C. Nunez-Lopez, *Phytopharmacology* **2018**, *20*, 589.

[2] a) K. Kwon, J. U. Kim, S. M. Won, J. Zhao, R. Avila, H. Wang, K. S. Chun, H. Jang, K. H. Lee, J. H. Kim, S. Yoo, Y. J. Kang, J. Kim, J. Lim, Y. Park, W. Lu, T. I. Kim, A. Banks, Y. Huang, J. A. Rogers, *Nat. Biomed. Eng.* **2023**, https://doi.10.1038/s41551-023-01022-4 ; b) D. Kireev, K. Sel, B. Ibrahim, N. Kumar, A. Akbari, R. Jafari, D. Akinwande, *Nat. Nanotechnol.* **2022**, *17*, 864.

[3] J. C. Hwang, M. Kim, S. Kim, H. Seo, S. An, E. H. Jang, S. Y. Han, M. J. Kim, N. K. Kim, S. W. Cho, S. Lee, J. U. Park, *Sci. Adv.* **2022**, *8*, 16.

[4] a) Y. Fang, Y. Zou, J. Xu, G. Chen, Y. Zhou, W. Deng, X. Zhao, M. Roustaei, T. K. Hsiai, J. Chen, *Adv. Mater.* **2021**, *33*, 2104178; b) S. V. Fernandez, D. Sadat, F. Tasnim, D. Acosta, L. Schwendeman, S. Shahsavari, C. Dagdeviren, *Phytopharmacology* **2022**, *24*, 75.

[5] a) N. Li, Z. Yi, Y. Ma, F. Xie, Y. Huang, Y. Tian, X. Dong, Y. Liu, X. Shao, Y. Li, L. Jin, J. Liu, Z. Xu, B. Yang, H. Zhang, *ACS Nano* **2019**, *13*, 2822; b) J. Li, Y. Long, F. Yang, H. Wei, Z. Zhang, Y. Wang, J. Wang, C. Li, C. Carlos, Y. Dong, Y. Wu, W. Cai, X. Wang, *Adv. Funct. Mater.* **2020**, *30*, 2002868.

[6] a) Y. Zang, F. Zhang, C.-a. Di, D. Zhu, *Mater. Horiz.* **2015**, *2*, 140; b) M. Yavarimanesh, H. M. Cheng, C. H. Chen, S. H. Sung, A. Mahajan, R. A. Chaer, S. G. Shroff, J. O. Hahn, R. Mukkamala, *npj Digital Med.* **2022**, *5*, 168.

[7] R. Herbert, H. R. Lim, B. Rigo, W. H. Yeo, *Sci. Adv.* **2022**, *8*, 12.

[8] a) C. M. Boutry, L. Beker, Y. Kaizawa, C. Vassos, H. Tran, A. C. Hinckley, R. Pfattner, S. Niu, J. Li, J. Claverie, Z. Wang, J. Chang, P. M. Fox, Z. Bao, *Nat. Biomed. Eng.* **2019**, *3*, 47; b) H. Ouyang, Z. Li, M. Gu, Y. Hu, L. Xu, D. Jiang, S. Cheng, Y. Zou, Y. Deng, B. Shi, W. Hua, Y. Fan, Z. Li, Z. Wang, *Adv. Mater.* **2021**, *33*, 2102302.

[9] Y. J. Hong, Y. Jeong, K. W. Cho, N. Lu, D. H. Kim, *Adv. Funct. Mater.* **2019**, *29*, 1808247.

[10] K. Meng, X. Xiao, W. Wei, G. Chen, A. Nashalian, S. Shen, X. Xiao, J. Chen, *Adv. Mater.* **2022**, *34*, 2109357.

[11] a) X. Liu, P. Xiong, L. Li, M. Yang, M. Yang, C. Mao, *Mater. Horiz.* **2022**, *9*, 1658; b) K. H. Ha, W. Zhang, H. Jang, S. Kang, L. Wang, P. Tan, H. Hwang, N. Lu, *Adv. Mater.* **2021**, *33*, 2103320.

[12] Z. Yi, Z. Liu, W. Li, T. Ruan, X. Chen, J. Liu, B. Yang, W. Zhang, *Adv. Mater.* **2022**, *34*, 2110291.

[13] Y. Liu, J. Li, S. Song, J. Kang, Y. Tsao, S. Chen, V. Mottini, K. McConnell, W. Xu, Y. Q. Zheng, J. B. Tok, P. M. George, Z. Bao, *Nat. Biotechnol.* **2020**, *38*, 1031.

[14] a) C. M. Boutry, A. Nguyen, Q. O. Lawal, A. Chortos, S. Rondeau-Gagne, Z. Bao, *Adv. Mater.* **2015**, *27*, 6954; b) E. Vahabli, J. Mann, B. S. Heidari, M. Lawrence-Brown, P. Norman, S. Jansen, E. De-Juan-Pardo, B. Doyle, *Adv. Healthcare Mater.* **2022**, *11*, e2200271.

[15] a) D. H. Kim, H. J. Shin, H. Lee, C. K. Jeong, H. Park, G.-T. Hwang, H.-Y. Lee, D. J. Joe, J. H. Han, S. H. Lee, J. Kim, B. Joung, K. J. Lee, *Adv. Funct. Mater.* **2017**, *27*, 1700341; b) Y. Li, N. Li, W. Liu, A. Prominski, S. Kang, Y. Dai, Y. Liu, H. Hu, S. Wai, S. Dai, Z. Cheng, Q. Su, P. Cheng, C. Wei, L. Jin, J. A. Hubbell, B. Tian, S. Wang, *Nat. Commun.* **2023**, *14*, 4488.

[16] a) Y. Zhang, N. Zheng, Y. Cao, F. Wang, P. Wang, Y. Ma, B. Lu, G. Hou, Z. Fang, Z. Liang, *Sci. Adv.* **2019**, *5*, eaaw1066; b) Y. Luo, M. R. Abidian, J.-H. Ahn, D. Akinwande, A. M. Andrews, M. Antonietti, Z.

**ADVANCED
SCIENCE NEWS**

www.advancedsciencenews.com

**NANO · MICRO
small**

www.small-journal.com

Bao, M. Berggren, C. A. Berkey, C. J. Bettinger, *ACS Nano* **2023**, *17*, 5211.

[17] Z. Yi, F. Xie, Y. Tian, N. Li, X. Dong, Y. Ma, Y. Huang, Y. Hu, X. Xu, D. Qu, X. Lang, Z. Xu, J. Liu, H. Zhang, B. Yang, *Adv. Funct. Mater.* **2020**, *30*, 2000477.

[18] Z. Liu, M. Cai, X. Zhang, X. Yu, S. Wang, X. Wan, Z. L. Wang, L. Li, *Adv. Mater.* **2021**, *33*, 2106317.

[19] S. K. Ghosh, D. Mandal, *Nano Energy* **2018**, *53*, 245.

[20] a) C. O'Connor, E. Brady, Y. Zheng, E. Moore, K. R. Stevens, *Nat. Rev. Mater.* **2022**, *7*, 702; b) S. F. Karkan, S. Davaran, R. Rahbarghazi, R. Salehi, A. Akbarzadeh, *J. Biol. Eng.* **2019**, *13*, 13.

[21] a) A. Natarajan, A. Pantelopoulos, H. Emir-Faronas, P. Natarajan, *Lancet Digital Health* **2020**, *2*, e650; b) M. T. La Rovere, G. D. Pinna, S. H. Hohnloser, F. I. Marcus, A. Mortara, R. Nohara, J. T. Bigger, A. J. Camm, P. J. Schwartz, *Circulation* **2001**, *103*, 2072.